Materials Science & Engineering A 772 (2020) 138662

Contents lists available at ScienceDirect

Materials Science & Engineering A

journal homepage: http://www.elsevier.com/locate/msea

Hydrogen environmentally assisted cracking during static loading of AA7075 and AA7449

Unai De Francisco *, Nicolas O. Larrosa, Matthew J. Peel

Department of Mechanical Engineering, University of Bristol, UK

ARTICLE INFO

Keywords:
4-point bending
AA7449
AA7075
Hydrogen environmentally assisted cracking
Microstructurally short cracking
Moist air

ABSTRACT

Some newer 7xxx aluminium aerospace alloys seem to be more sensitive to hydrogen environmentally assisted cracking (HEAC) in moist air than older alloys. This investigation compares the relative propensity of new (AA7449) and old (AA7075) alloys to cracking during static loading in warm, moist air (80°C, 85% relative humidity). The surface stress was held below yield via 4-point bend tests performed using small rigs that permitted ongoing monitoring for small scale surface cracking. Both alloys exhibited HEAC but large cracks formed much more quickly in AA7449 and at lower stresses. The AA7449 alloy rapidly formed cracks at surface stresses as low as 200 MPa, where one sample nucleated a crack greater than 5 mm after only 704 h of exposure. In contrast, AA7075 samples at 250 MPa did not form macroscopic cracks greater than 5 mm within 1600 h of exposure. The importance of many microstructural features and the differences in crack morphology of both alloys were analysed using optical and electron microscopy. Crack propagation in AA7449 was found to be facilitated by the ability of cracks to grow via tortuous paths and overcome barriers, such as triple junctions and unfavourably oriented grain boundaries. This resulted in fewer, much longer cracks in this alloy for the same load and environmental conditions.

1. Introduction

Hydrogen environmentally assisted cracking (HEAC) is a widespread problem affecting many high strength engineering alloys including steels [1], β-Ti alloys [2] and aluminium alloys. HEAC is caused by a combination of mechanical loading and chemical reaction. Hydrogen evolved at the alloy surface is absorbed, subsequently degrading the fracture resistance. Several mechanisms have been proposed for the hydrogen embrittlement (HE) mechanisms degrading the fracture resistance in different alloys, including: the formation of brittle hydride phases [3], hydrogen enhanced decohesion (HEDE) [4], adsorption-induced dislocation emission (AIDE) [5] and hydrogen enhanced localised plasticity (HELP) [6].

Structural high strength aluminium alloys from the 7xxx series are specifically susceptible to HEAC in aqueous environments (including moist air and water-based ionic solutions) [7]. In this case, the ingress of hydrogen to the alloy occurs via the reaction of the water/electrolyte with the alloy surface. During static loading, hydrogen subsequently diffuses to regions subjected to a high hydrostatic stress [8]. Eventually, cracks may nucleate and propagate along sufficiently embrittled grain boundaries and subsequently arrest. After sufficient hydrogen ingress, the crack grows again and the process is repeated, resulting in discontinuous intergranular crack growth [9]. This is consistent with the intergranular fracture surfaces of statically loaded 7xxx alloys, which typically display parallel striations (linked with ductile blunting during crack arrest) [7,9,10]. The striations are usually equispaced (between 200 and 500 nm separation) and perpendicular to the crack propagation direction [9]. The crack growth rate is controlled by the slowest step in the process of accumulating hydrogen at the critically stressed grain boundaries. Therefore, it may be limited by (a) the transport of hydrogen containing species to the alloy surface (particularly in gaseous environments), (b) the reaction rate at the alloy surface or (c) the diffusion rate of hydrogen within the alloy [11]. These three steps are temperature dependent and follow Arrhenius kinetics. Thus, HEAC crack growth rates also increase with temperature exponentially [7,12].

The HE mechanism causing fracture in 7xxx alloys is unclear. Holroyd et al. advocate in their extensive literature review that the embrittling mechanism is the formation of aluminium hydride (AlH3) at the grain boundaries [9]. This is based on findings by Ciaraldi et al., where AlH3 was diagnosed to be present at the intergranular surfaces of

* Corresponding author.
E-mail address: ud13050@bristol.ac.uk (U. De Francisco).

https://doi.org/10.1016/j.msea.2019.138662
Received 28 August 2019; Received in revised form 8 November 2019; Accepted 9 November 2019
Available online 14 November 2019

peak aged Al-5.6Zn-2.6 Mg during slow strain rate tests and bend tests [13].

The behaviour of 7xxx alloys differs considerably in moist air and aqueous solutions. Aqueous solutions cause extensive corrosion and localised pitting, via (a) the dissolution of anodic particles and strengthening precipitates (Mg_2Si and η) and (b) the peripheral pitting at the interface of noble Al–Cu–Fe particles [14]. In contrast, 7xxx alloys in moist air do not display thick corrosion films or the dissolution of particles [10]. Thus, lower reaction rates result in less hydrogen ingress and lower crack growth rates. Despite this fact, HEAC has been reported in 7xxx series alloys at relative humidities as low as 10% [9]. It has been identified that the relative humidity has a limited effect on the crack growth rate of 7xxx alloys during stage I cracking (crack growth rate dependent on the stress intensity factor, K_I) [15]. However, there is a linear dependence between the relative humidity and the crack growth rate during stage II cracking (K_I independent crack growth rate) [16].

Varying the composition and the ageing condition of 7xxx alloys can have a significant effect on the HEAC crack growth rates. Increasing the Cu content of 7xxx alloys has been correlated with a decreased sensitivity to HEAC in moist air and aqueous solutions [7,17,18]. Young et al. list a number of proposed mechanisms for the effect of Cu on HEAC including: (a) the promotion of homogeneous deformation by altering the precipitates, thus preventing the rapid diffusion of hydrogen via coarse slip paths; (b) an increase in the electrochemical nobility of the precipitates; (c) an increase in the hydronium ion reduction rate and subsequent hydrogen recombination at Cu rich particles; (d) increased hydrogen solubility leading to beneficial trapping and a lower diffusible hydrogen content [7]. In contrast, the influence of Mg and Zn on HEAC has not been investigated in detail, but a higher Zn content has been correlated with an increased sensitivity [8,19].

It has been recognised that increased ageing results in a decreased susceptibility to HEAC [7,20–24]. Averaging results in coarser and more widely spaced precipitates (η' and η). Similar to the effect of composition, the effect of overaging on HEAC has been linked to various mechanisms: (a) coarser precipitates are more resistant to shearing and can prevent coarse slip lines that facilitate hydrogen diffusion [24]; (b) coarse incoherent η precipitates act as irreversible hydrogen trap sites and reduce the diffusible hydrogen concentration [25]; (c) overaging results in a higher Cu content in the strengthening precipitates and consequently increases their nobility [20]. Alternative ageing processes have been developed for 7xxx alloys with the aim of maximising the strength and the resistance to HEAC, such as secondary ageing [20] and retrogression and reaging [26].

1.1. Motivation and aims

7xxx aluminium alloys are typically used for airframe components because of their high strength to weight ratio [20]. In-flight loading environments with a high relative humidity can lead to HEAC and premature failure of these components [27]. Consequently, it is necessary to understand the behaviour of these alloys in moist air for the prognosis and development of airframe components and the optimisation of crack detection strategies.

Fracture mechanics tests on double cantilever beam (DCB) specimens on a wide range of 7xxx alloys in different environments have been reported [7,10,15,16,28,29]. However, these specimens neglect crack initiation and microstructurally short cracking (MSC), despite these stages dominating the environmentally assisted cracking lifetime of components [30]. Recent developments on the 7xxx alloys have led to a higher fracture toughness by increasing the Zn/Mg ratio. Further, modifications in the dispersoid alloying elements have reduced the quench sensitivity and allowed better control of the microstructure [31]. However, this new generation of 7xxx series alloys has been found to be more susceptible to HEAC in moist air, presumably due to the compositional changes (higher Zn/Mg ratio and lower Cu content) [32]. Consequently, the HEAC behaviour of these aluminium alloys in moist air must be investigated in detail.

The primary aim of this work is to compare the propensity to form short cracks during static loading of samples made from two rolled alloys with different Zn/Mg ratios: AA7449 (high Zn/Mg) and AA7075 (low Zn/Mg). To this end, 4-point bend tests were performed on samples of each alloy in warm, moist air. Smooth samples were statically loaded at different stress levels and monitored in a controlled environmental chamber. This allowed the determination of the time required for microstructurally long cracks to evolve as a function of the stress level for each alloy. Testing of both alloys was performed in two different orientations relative to the microstructure, to identify how MSC is influenced by the grain morphology. This work also aims to determine the key differences in behaviour between the sensitive (AA7449) and insensitive (AA7075) alloys at different stress levels. By carrying out extensive microscopy, the morphology and evolution of cracks relative to the microstructure was characterised and correlated to the failure times of the bend specimens.

2. Experimental methods

4-point bending provides a simple way to load smooth, uncracked samples in an aggressive environment, with the advantage that the tensile stresses are uniform between the inner pins [33]. The tensile surface, which is more prone to crack nucleation, can be easily monitored by visual inspection or microscopy. By inserting the rigs in a controlled environmental chamber and surveying the samples at regular intervals, the time to failure of the samples was determined.

2.1. Material

The materials used in this study were AA7075-T651 and AA7449-T7651 whose compositions are shown in Table 1. The AA7449 contains more Zn, has tighter tolerances on Fe/Si and contains Zr. The T651 and T7651 tempers are achieved by solution heat treating, stress relieving by stretching and artificially ageing to a peak aged and an overaged condition respectively. Both materials were obtained as rolled 80 mm thick plate at the aforementioned tempers. The tensile properties of both materials were obtained by tensile testing along the short transverse (*ST*) axis. The results are summarised in Table 2.

2.2. Sample preparation

The specimens used for bending were cut using electrical discharge machining to dimensions of 80 × 10 × 2 mm. The specimens were cut in two different orientations relative to the rolling axes as illustrated in Fig. 1. The specimen orientations were chosen such that the tensile axis is aligned with the *ST* direction (most susceptible to HEAC [15]).

The samples were polished at the tensile face and the two adjacent long edges. The polished edges and maximum tension surface are labelled in Fig. 2. The required surface finish was achieved by successive grinding with SiC abrasive paper, followed by polishing using diamond paste and colloidal silica. The specimens were cleaned in between polishing steps with a 3 min ultrasonic bath in acetone and were later immediately blow-dried. After the final polishing step, the specimens were rinsed with acetone and immediately blow-dried. This process was strictly followed to minimise scatter arising from any effects of surface quality on crack nucleation.

2.3. Loading

The specimens were loaded using the 4-point bend rig illustrated in Fig. 2. The loading pins of the bend rig were painted with an epoxy primer to prevent galvanic corrosion during exposure. The samples were loaded to a surface stress between 100 MPa and 450 MPa. The upper value is 50 MPa below the yield strength of the AA7449 but 16 MPa above that of the AA7075 (see Table 2). Loading was displacement

Table 1
Composition of alloys in weight percent maximum unless shown as range (from active standard ASTM B209M).

Alloy	Zn	Mg	Cu	Fe	Si	Mn	Cr	Ti	Zr + Ti
7075	5.1–6.1	2.1–2.9	1.2–2.0	0.5	0.4	0.3	0.18–0.28	0.2	
7449	7.5–8.7	1.8–2.7	1.4–2.1	0.15	0.12	0.2			0.25

Table 2
Tensile properties of AA7449-T7651 and AA7075-T651. σ_{ys} = Yield Stress, σ_{uts} = Ultimate Tensile Stress, ε_f = Strain to Fracture.

Alloy	Axis	σ_{ys} (MPa)	σ_{uts} (MPa)	ε_f (%)
7075-T651	ST	434	523	7.45
7449-T7651	ST	501	561	8.26

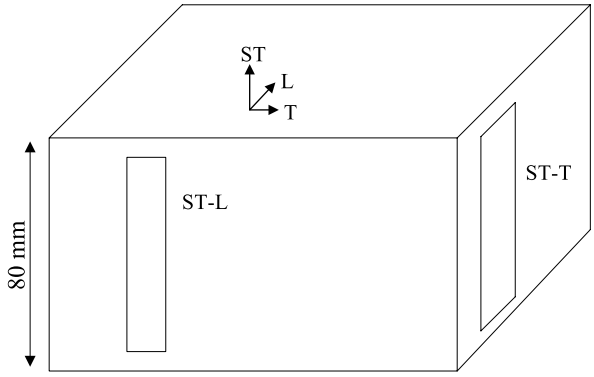

Fig. 1. Diagram showing the 2 tested sample orientations. *L* = Longitudinal, *T* = Transverse, *ST*= Short Transverse.

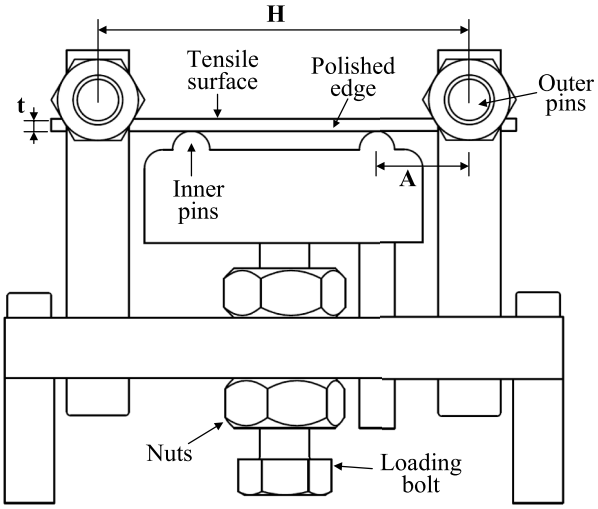

Fig. 2. Diagram of the 4-point bend rig indicating the polished specimen surfaces.

controlled using a *Shimadzu* 1 kN testing machine to apply the required displacement on the loading bolt. Loading was increased slowly to ensure the desired stress was not exceeded. When the required displacement was obtained, the two nuts on the loading bolt were slowly tightened against the base plate, making sure to alternate tightening to minimise the bias to either side. The displacement of the loading bolt is given by Ref. [33].

$$y_{pin} = \frac{\sigma A(3H - 4A)}{3Et}, \quad (1)$$

where σ is the required maximum tensile stress (nominally uniform in between the inner pins), *H* is the spacing between the outer pins (60 mm), *A* is the spacing between the outer pins and the inner pins (15 mm), *t* is the specimen thickness (2 mm) and *E* is the Young's modulus of the aluminium (71 GPa).

2.4. Environmental exposure

The bent specimens were exposed to an environment of 80°C and 85% relative humidity (RH) in a *Vötsch VC 7034* electronically controlled chamber. The high temperature was chosen to speed up the crack growth rate, as the HEAC of 7xxx series aluminium alloys has been identified to follow Arrhenius kinetics [9]. A higher temperature was not applied, as the risk of further precipitate ageing was deemed too high. Hardness testing before and after exposure confirmed the ageing condition of the materials was not altered by the 80°C temperature.

2.5. Microscopy

The primary microscopy method was light microscopy using a conventional setup. Some samples were subject to a more extensive examination over the entire tensile surface using an *Alicona InfiniteFocus* microscope with automatic rastering, a large depth of field and space to accommodate even large loading rigs. This permitted the quantification of short cracks and other surface defects over time in greater detail even on loaded samples with a bent surface.

Crack analysis was done on unetched samples in order to maximise contrast. Where necessary, the microstructure of AA7075 was made visible by immersing the samples in Keller's reagent (2 ml HF, 3 ml HCl, 5 ml HNO_3, 190 ml water) or Weck's reagent (4g $KMnO_4$, 1g NaOH, 100 ml water) for 20 s. For AA7449, immersion in Weck's reagent was found to more clearly reveal the microstructure.

Electron backscatter diffraction (EBSD) was performed on a small number of cracked sections with the aim of correlating the crack growth behaviour of microscopic cracks with the surrounding microstructure. This was done using a *Zeiss Sigma HD VP* field emission SEM with *EDAX* EBSD. Additionally, the composition of coarse constituent particles was analysed using energy dispersive X-ray spectroscopy (EDX), with the same *Zeiss* microscope fitted with *Octane Plus* EDX.

Many samples fractured completely after the appearance of macroscopic cracks. The fracture surfaces of some samples were explored using scanning electron microscopy (SEM) with a *TM3030 plus* microscope.

Four main strategies were employed to evaluate the cracking behaviour:

1. In order to evaluate the time to failure, samples were removed from the chamber at regular intervals to make a visual inspection of the cracks in the tensile surface. Once any single macroscopic surface crack larger than 5 mm was found, the samples were unloaded and stored in a desiccator with silica gel. This was recorded as the time to failure.
2. A subset of samples were regularly removed, as above, but additionally had their tensile surface imaged and recorded using the Alicona microscope while still loaded. This provided additional quantitative information but was time demanding. Further, these samples had to be polished to only a 3 μm surface roughness, as samples with a smoother surface finish could not be imaged in the Alicona due to the high reflectivity of the surface. Samples with a

3 μm surface finish were generally identified to propagate cracks faster. For example, samples of AA7449 subjected to 300 MPa and polished to a colloidal silica finish fractured after 251 (ST-T) and 343 (ST-L) hours. Otherwise identical samples left at a 3 μm surface finish fractured after 94 (ST-T) and 132 (ST-L) hours. This may be due to differences in the passive surface layer or differences in the surface area due to the presence of asperities. Nevertheless, the relationship between the crack path and microstructure is not expected to be altered.

3. Several fully polished samples were unloaded before macroscopic cracks longer than 5 mm appeared on the surface and had a 30 × 10 mm central region of their tensile surfaces examined in detail using a conventional microscope. Four samples were analysed in order to determine how the initial nucleation and growth of cracks depends on the alloy, stress and exposure time:
   - AA7075 (ST-L) at 300 MPa for 161 h,
   - AA7449 (ST-L) at 300 MPa for 161 h,
   - AA7449 (ST-L) at 200 MPa for 161 h,
   - AA7449 (ST-L) at 200 MPa for 329 h.
4. In order to obtain a better idea of the 3D distribution of cracks, a few samples were subjected to sequential polishing and imaging. Coupons ranging in size between 12.5 × 10 mm and 30 × 10 mm were cut from the maximum tension region of each sample (Fig. 3). Polishing was performed using the process described in section 2.2. After each polishing step, the cracked sections were imaged using an optical microscope, the thickness of the coupon was measured to determine the amount of surface removed (the average step was approximately 20 μm) and the process repeated. An example of a crack imaged at three depths is presented in Fig. 3. A sample of AA7075 (ST-L), loaded for 481 h at 350 MPa, was polished on the tensile surface (Region A, Fig. 3). Another sample of AA7449 (ST-T), loaded for 161 h at 200 MPa was also polished on the tensile surface (Region A). Additionally, for some samples of AA7449, sequential polishing was performed from the long edge of the samples - Region B in Fig. 3 (a) - in order to more easily detect subsurface cracks.

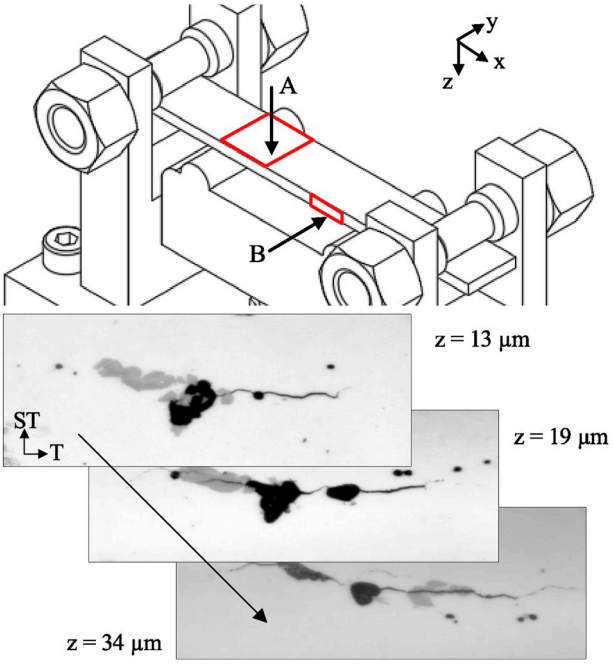

Fig. 3. A schematic showing the directions of sequential polishing along with example images of sequential polishing steps through a crack in AA7075 associated with Mg_2Si particles (black) and Al–Cu–Fe particles (grey).

3. Results

3.1. Microstructure

The microstructures of as-received AA7075-T651 and AA7449-T7651 are shown in Fig. 4 and are notably different. AA7075 is seen to contain a much larger quantity of constituent particles (Al–Cu–Fe and Mg_2Si), as expected form the higher Fe and Si impurity content given in Table 1. The microstructure of AA7075 comprises elongated recrystallised grains along the longitudinal (rolling) direction, some being longer than 1 mm. The majority of grains in AA7449 contain an extensive substructure, showing a lower recrystallisation fraction. This difference can be associated to the difference in dispersoid alloying elements; specifically the use of Zr instead of Cr for the recent AA7449. Zr has a low solubility in aluminium, which results in the formation of Al_3Zr particles during the initial homogenisation heat treatment [34]. Al_3Zr particles act to slow recrystallisation during solution heat treatment by pinning dislocations and grain boundaries [35]. Zr-bearing dispersoids are known to be more effective than Cr- and Mn-bearing dispersoids in 7000 series alloys, resulting in a lower recrystallised fraction and a lower quench sensitivity [36]. Additionally, AA7449 contains more equiaxed recrystallised grains of a range of sizes and shapes. The coarse recrystallised grains, generally free of substructure, are often grouped in succession along the longitudinal direction; presumably tracking the grain boundaries of the original, deformed grains.

3.2. Fracture surfaces

Examples of typical intergranular HEAC fracture surfaces of AA7449-T7651 and AA7075-T651 in moist air have been shown in Fig. 4(c) and (d). The topography of the fracture surfaces were consistent with the microstructures of each alloy. This is clear by comparing the etched microstructure of the AA7449 in Fig. 4(b) with the fracture surface in Fig. 4(c). The topography of the fracture surfaces in the AA7449 can be seen to vary considerably from region to region depending on the grains at either side of the interface. Several matching features have been labelled including: A) a coarse recrystallised grain and B) a region with subgrains. A result of note in the AA7449 was the presence of prominent secondary cracks at the interface of recrystallised grains (see Fig. 4(c)). In comparison, the fracture surfaces in the AA7075 had a uniform appearance as shown in Fig. 4(d), in accord with the unvaried long recrystallised grains.

The fracture surfaces did not display parallel striations that are typically observed in the intergranular HEAC facets of 7xxx alloys [9].

3.3. Time to failure of bend specimens

Fig. 5 shows the time to failure (i.e. surface crack length >5 mm) of both alloys as a function of surface stress and sample orientation (ST-T and ST-L, Fig. 1). The time to failure is strongly dependent on stress and alloy but only weakly affected by the orientation of the samples. As expected, the AA7075 (low Zn/Mg ratio) took much longer to grow large cracks compared to AA7449 when subject to the same stress.

It is useful to separate the results into four approximate groups in terms of the applied stress:

1. $\sigma > 350$ MPa: Fracture in AA7449 at high stress was rapid, requiring only 24–131 h. The time to failure appears independent of stress in this regime although the time resolution (1 check per day) is relatively coarse. In AA7075, at the same stress, cracks nucleated and grew to 5 mm within 345–779 h, indicating lower sensitivity to HEAC. There is some evidence of the time to failure increasing with stress although the effect is mild. It is possible this arises from local plasticity as the yield strength is around 434 MPa for this alloy.
2. 200 $\leq \sigma < 350$ MPa: At moderate loads, the delay to failure of AA7449 decreases roughly linearly with stress from around 24 h at

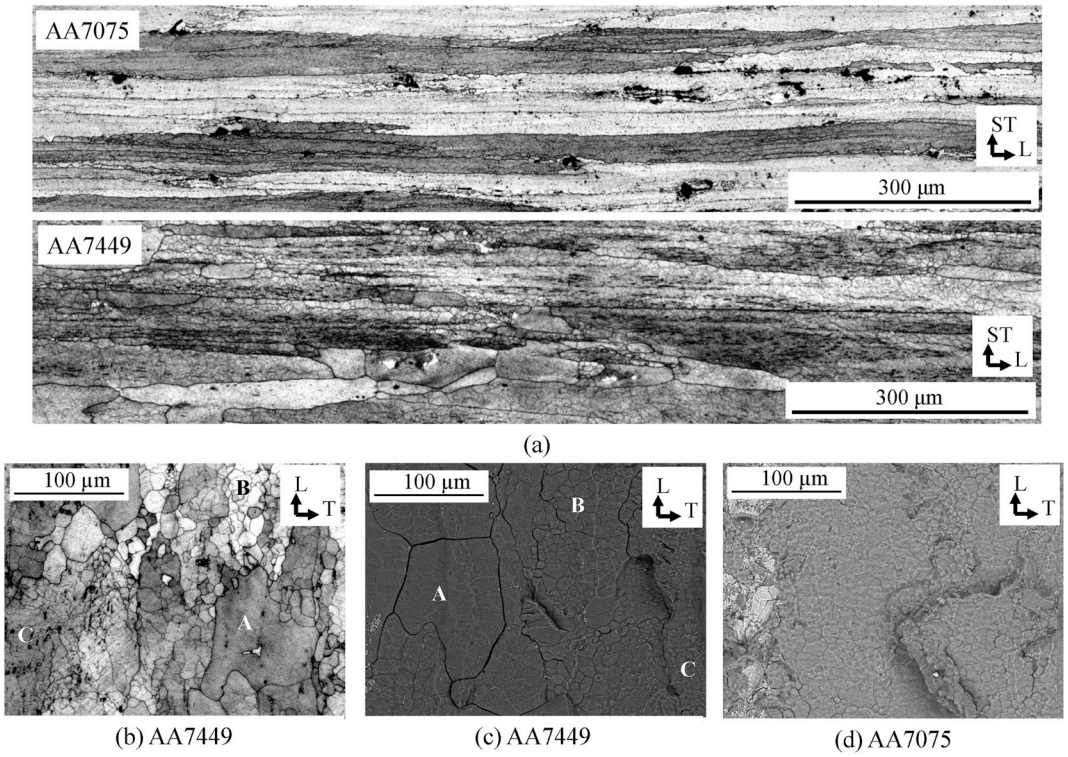

Fig. 4. (a) Etched microstructures for both alloys on the ST-L plane showing the pancaked grain structure, the differing degree of substructure between the two and the greater number of coarse Mg_2Si and Al–Cu–Fe particles in the AA7075-T651. (b) Etched microstructure of AA7449-T7651 on the T-L plane. (c) SEM fractograph of AA7449-T7651 showing the intergranular facets corresponding to different grains. Similar features in (b) and (c) were labelled as A (coarse recrystallised grains), B (regions with small subgrains) and C (coarse grains with some low angle grain boundaries). (d) SEM fractograph of AA7075-T651 showing a coarse cracked Al–Cu–Fe particle and a broad intergranular facet.

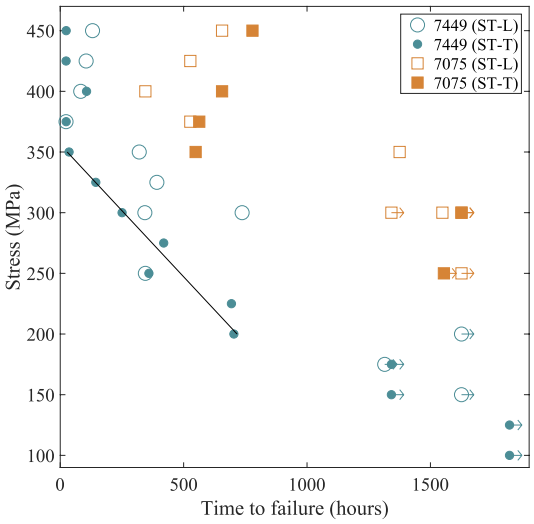

Fig. 5. Graph of the time to failure vs. maximum tensile stress. The arrows indicate samples which were unloaded before failure (crack lengths < 5 mm). The time to failure is correct within ±24 h.

350 MPa up to 750 h at 200 MPa. A clear trend is evident for ST-T samples, indicated by a line in Fig. 5, although this is less clear for the ST-L samples. In the AA7075, most (4 from 5) samples did not manage to produce a 5 mm crack in 1400–1600 h.

3. 150 $< \sigma <$ 200 MPa: At low stresses cracks are found to nucleate in the AA7449 but could not grow to 5 mm length even after 1600 h of exposure. Opportunities for very long exposure times were limited but two samples of AA7449 subjected to 175 and 150 MPa in the ST-T direction were found to contain macroscopic cracks (>5 mm) after 2750 h of exposure. No AA7075 samples were tested at these stresses given the lack of long cracks at higher stresses.
4. $\sigma <$ 125 MPa: At very low stresses a significant transition occurred in the AA7449 - no cracks could be seen on the surface of samples even after exposure times in excess of 1800 h. This is indicative of an apparent threshold stress for crack nucleation.

The results confirm that AA7449 has a much greater propensity to form long cracks compared to AA7075 under the same conditions.

3.4. Crack length distributions

Before examining the details of crack growth and the relationship to the microstructure it is helpful to examine the differences in crack distributions between the two alloys. These could only be accurately measured on unloaded samples and as such there are limited data sets and none show the evolution as a function of time. Fig. 6 presents a strip plot of the length of all cracks visible on the surface at three different stress/time combinations. Plots A and B are representative of crack size distributions in AA7075 and AA7449, respectively, before any large (1–5 mm) cracks have been able to form. In both cases the distributions are, broadly speaking, symmetrically distributed around the mean. The AA7075 is characterised by a small crack size (mean = 57 μm) and a tight clustering (standard deviation = 25 μm). Although AA7449 was held at a lower stress than the AA7075, it has more, larger cracks (mean = 224 μm) that show a much greater spread (s.d. = 95 μm) than the older alloy. Plot C is identical to B except that the stress has increased to 300 MPa. There are in fact fewer cracks in this sample compared to B despite the higher stress. Nevertheless, the crack lengths in both sets are similarly distributed. The exception is a single crack in plot C that has grown to 1.1 mm in length. It is reasonable to conclude this crack would

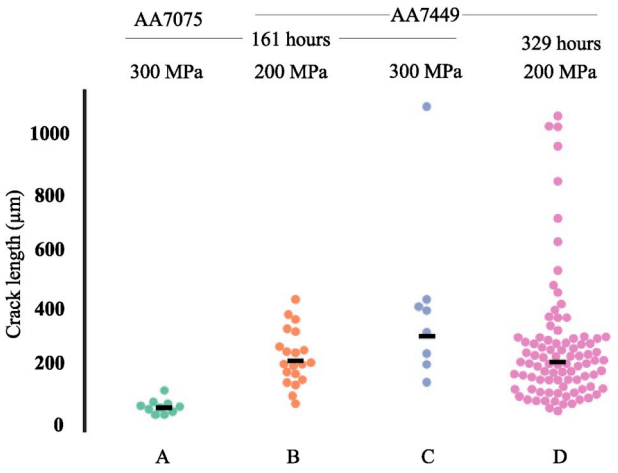

Fig. 6. Swarm plot showing the lengths of surface cracks, as viewed from the tensile surface for samples loaded in the ST-T orientation, as a function of alloy, tensile stress and exposure time. The black markers are estimates of the population mean after removing outliers (more than 2 std deviations from the sample mean).

have rapidly extended to the 5 mm failure criterion in a short time. In a similar vein, plot D is identical to B except that the exposure time is now much longer (329 h). It is clear that a large number of additional cracks were able to nucleate and grow. This more clearly demonstrates the distribution of cracks sizes in AA7449: a large population of cracks 100–300 μm long with a small number (≈ 10%) of much larger cracks (400–1000 μm).

Qualitative observations based on optical microscopy on the loaded samples support the quantitative crack length data. For both alloys, the number of visible cracks on the surface increased with time. These rapidly grew to a length consistent with the distributions shown in Fig. 6 (i.e. 50–100 μm for AA7075, 100–300 μm for AA7449) but most then arrested, or at least slowed significantly. A small subset of cracks were able to grow outside this size range and, once formed, growth seemed to be rapid and led to failure. At low stresses (<350 MPa for AA7075, <200 MPa for AA7449), the time for the abnormally long cracks to form was much greater and so there was more time for additional short cracks to form. As a result, samples that were removed before a large crack could be formed were characterised by large crack densities - sometimes exceeding 150 cracks per mm^2 for the AA7075, which could be exposed to high stresses for extended periods of time without failure.

3.5. Crack growth

It is instructive to compare the detailed growth behaviour of a crack from each alloy. In both alloys, the early period of exposure was characterised by the formation of black speckles on the surface, presumably hydrogen blisters in the surface oxide [37], that preferentially formed along grain boundaries. Subsequently small cracks would become visible, again tracking the grain boundaries. Nucleation was typically delayed and cracks tended to become visible when already tens or hundreds of micrometers in length. Since both cracking and blistering are associated with grain boundaries they are clearly spatially correlated but the degree of mechanistic interaction between them is unclear.

Fig. 7 plots the length of two cracks with time and includes micrographs of the crack in AA7075. It can be seen that after nucleation, the crack grew steadily until it reached a length of approximately 185 μm after 630 h of exposure. Beyond this point, the crack growth rate decreased significantly and, after two small bursts in crack growth, eventually arrested completely. The crack was oriented perpendicular to the applied stress and remained essentially straight throughout. Fig. 8 includes an EBSD map of the final crack. It is clear that the crack followed a grain boundary and crack arrest occurred at the three labelled grain boundary triple junctions. There was some minor crack branching, perhaps accounting for the small growth after initial arrest, but the crack appears to be unable to propagate along boundaries poorly oriented with respect to the applied stress. This behaviour was observed for the majority of cracks in samples of AA7075, where most cracks did not propagate beyond 100 μm.

Growth in AA7449 was rather different. The crack was only observed after 262 h, when it was already 200 μm in length, suggesting rapid growth after nucleation. The crack was then stable when observed again after 309 h but grew rapidly to 300 μm after 331 h. Growth continued until the test was stopped due to another crack causing failure. The EBSD map of the crack (Fig. 8) indicates the crack stopped at grain boundary triple junctions, labelled as **A** and **C**. The period of slow growth can be correlated with the crack being at point **B**, where the grain boundary was approximately at 45° from the tensile axis. The unfavourable orientation of the boundary relative to the loading direction, resulting in

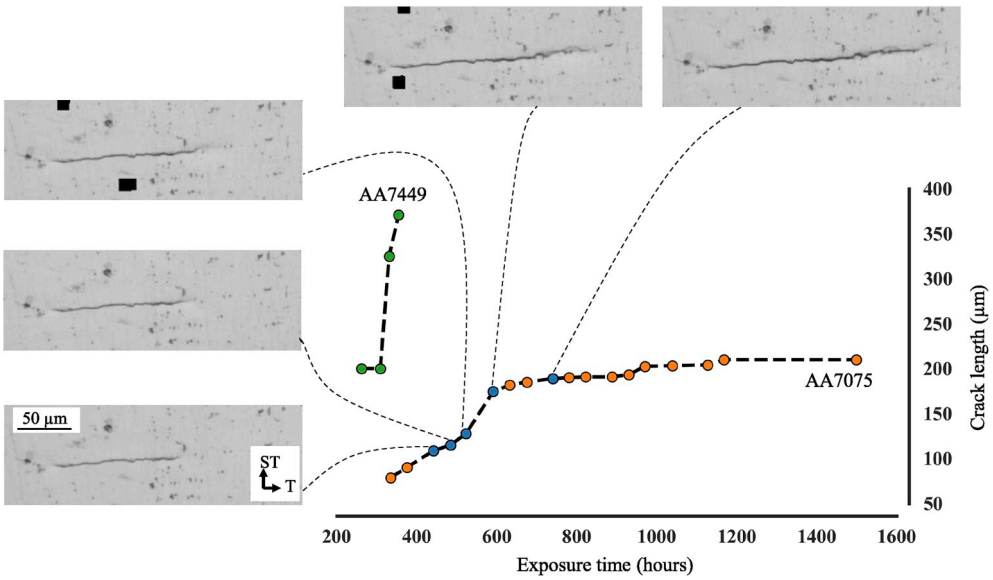

Fig. 7. Examples of growth behaviour of cracks in AA7075 and AA7449, in the ST-L orientation and subjected to 300 MPa. The plot is tagged with micrographs showing the evolution of the crack in the AA7075. In each case, no crack was observed prior to the earliest shown exposure time.

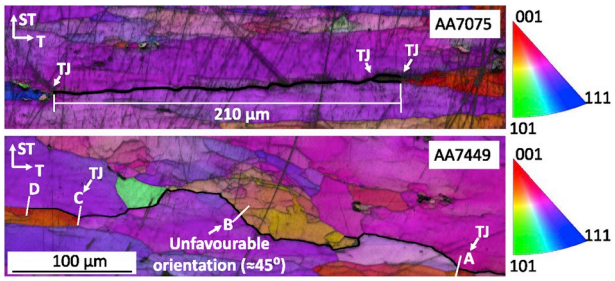

Fig. 8. EBSD maps of similar length cracks in AA7075 and AA7449 (corresponding to Fig. 7) both subjected to a surface stress of 300 MPa. In each case the crack path is shown with a black line as it is otherwise not visible in the map. Grain boundary triple junctions along the crack path have been labelled as **TJ**. The crack in the AA7449 was detected after 262 h of exposure with a length from point **A** to point **B**. The crack was unchanged after 309 h exposure but had grown to A-C after 331 h and A-D after 355 h.

a lower resolved stress normal to the grain boundary, would likely slow growth.

These observations are representative of the morphology and growth of cracks in AA7075 and AA7449 at stresses above 200 MPa. Cracks in AA7075 grew slowly, in straight lines, almost perfectly perpendicular to the tensile axis and came to a complete arrest before reaching a large size. In contrast, cracks in AA7449 grew rapidly, following tortuous paths, and were not observed to arrest completely after extended exposure times.

In AA7449, crack growth was rapid and primarily occurred by the progression of a single dominant crack even at low stress. In AA7075, only a limited number of cracks grew to a macroscopic size >5 mm and only at stresses above 350 MPa. The few cracks which grew to a larger size were segmented and grew by the coalescence of multiple short cracks. Samples subjected to a low stress for extended periods of time contained large populations of cracks. Thus, large growing cracks approached and coalesced with other existing cracks. This differs from the main crack growth mechanism exemplified in Fig. 9. Short cracks were seen to arrest at a triple junction, or similar feature, and then induce the nucleation of a different short crack nearby, frequently at a

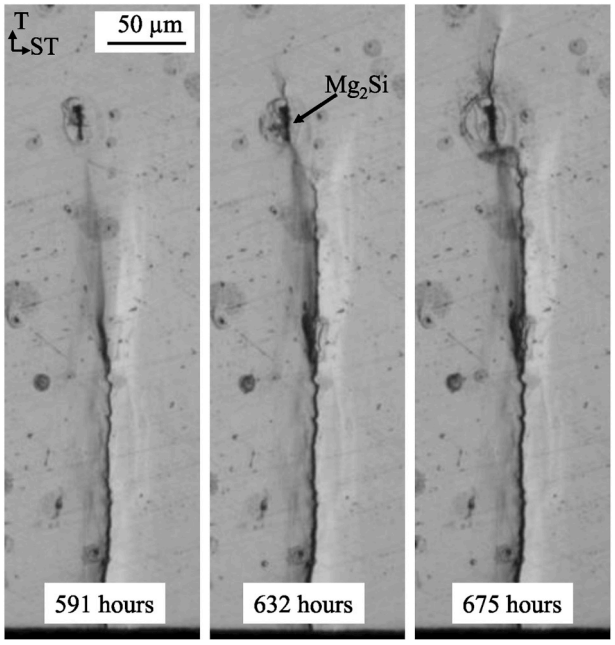

Fig. 9. Micrographs showing the evolution of a crack along the tensile surface of a sample of AA7075-T651 (ST-L) subjected to 350 MPa.

coarse cracked Mg_2Si particle. This is clear in Fig. 9, where a crack approaches a particle from below but then comes to a halt. A new crack starts at the nearby Mg_2Si particle and continues upwards with a ligament of material remaining between the old crack tip and the new crack. The ligaments from the segmented cracks prevented large cracks from opening up easily and slowed crack growth. Once the total sequential crack length was longer than 2–3 mm, the ligaments were ruptured, the cracks coalesced into a single longer crack and the samples failed after a short time. An example is shown in Fig. 10, which reveals a segmented crack in four distinct sections with small ligaments between them. A smaller, separate crack can also be seen some distance away from the crack tip. The ligaments hold the crack segments together and ensure a small crack mouth opening displacement (CMOD) despite the large overall crack length. A short time later, the microscopic ligaments ruptured and the CMOD increased drastically, ensuing rapid failure. The large ligament between the widely separated cracks was too much to overcome and remains between the two. Presumably the two crack tips are heavily shielded by each other and further growth at the shown ends would be unlikely. Complete fracture occurred only in samples subjected to high stress (>350 MPa), where the large ligaments could be ruptured and sections along the compressive surface displayed microvoid coalescence from overload rather than HEAC.

3.6. Microscopy: sequential polishing

A 12.5 × 10 mm coupon of AA7075 was sequentially polished from the tensile face to characterise the distribution of cracks as a function of depth below the surface. In this sample (350 MPa, 481 h) six cracks were detected along the tensile surface prior to polishing. After sequential polishing to a total depth beyond 100 μm, fifteen more cracks were detected below the surface that had previously been undetectable. Similarly, for a 30 × 10 mm coupon of AA7449 (200 MPa, 161 h) twenty cracks were initially visible from the maximum tension surface. Further polishing to a depth of 85 μm below the surface revealed seventy-four more cracks. This indicates that crack nucleation often occurs subsurface for both alloys, with only a subset of cracks penetrating to the upper surface, despite the greater stress and more direct exposure to the environment.

Fig. 11 illustrates images of etched cracked sections at a depth of 60 μm from the tensile surface of the coupon. The cracks shown are representative of the majority of cracks, which had lengths ranging from 20 to 70 μm. The majority of these subsurface cracks (19/21 cracks in this case) were located in the proximity (within 1 μm) of coarse Mg_2Si/Al–Cu–Fe particles and often traversed through them. From the surface observations, surface Al–Cu–Fe particles were only seen to fracture if they were close to the path of large macroscopic cracks, where local plastic deformation was presumably extensive. In contrast, Al–Cu–Fe particles close to even small subsurface microcracks were found to be cracked. This suggests that a degree of constraint, leading to triaxial stresses, is required for these particles to crack. The large degree of correlation between cracks and particles suggests constituent particle cracking plays a role in nucleating new microcracks, leading to more cracking in the subsurface region.

Several samples of AA7449 were sequentially polished and etched from the long edge (see Fig. 3(a), example B), with the aim of assessing the influence of the microstructure on crack growth. Fig. 12 illustrates five etched cracked sections in samples of AA7449. Fig. 12(a) and (b) depict two large cracks (>400 μm) while Fig. 12(c)–(e) present smaller cracks (<200 μm). As noted previously, cracks in AA7449 are more tortuous than those in AA7075 and often continue along poorly oriented boundaries or past triple junctions that would stop cracks in the older alloy. Consistent with the findings in AA7075, it was observed that most cracks in AA7449 also appeared to nucleate subsurface. Only one of the cracks in Fig. 12 has penetrated to the upper tensile surface. It is likely that the observed behaviour in Fig. 7, i.e. the sudden appearance of a long crack that then grows rapidly, is due to the very short cracks

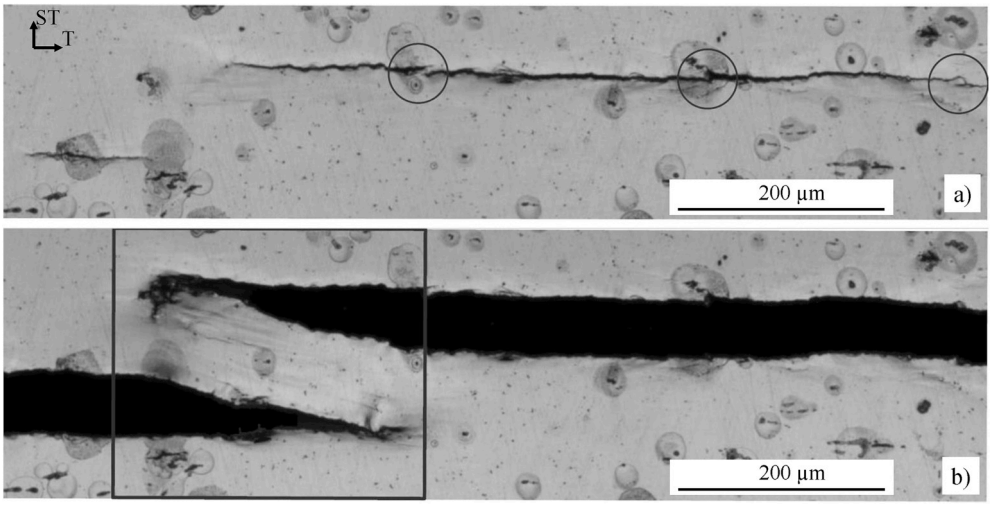

Fig. 10. Micrographs of the same surface crack in of AA7075 (ST-L) subjected to 350 MPa just before and just after crack coalescence. The circles in a) indicate short metal ligaments between short cracks, that subsequently rupture, forming a single crack in b). The box in b) indicates the location of a large ligament which did not rupture due to the large separation of the crack segments.

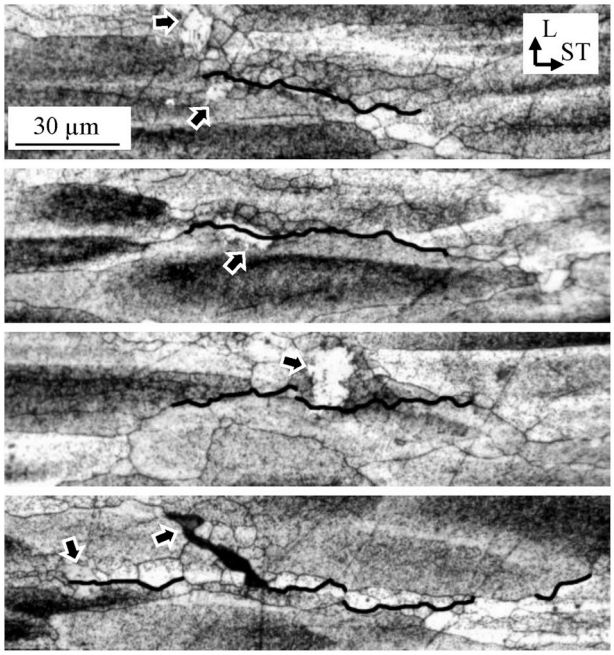

Fig. 11. Images showing the etched microstructure of cracked sections at a depth of 60 µm from the tensile surface of a sample of AA7075 (ST-L) subjected to 350 MPa during 481 h. Sequential polishing was done from the upper surface, downwards (Region A, Fig. 3) so the cracks have the same orientation as shown previously. The cracks are outlined with black lines to improve clarity. The constituent particles are indicated by arrows (black particles = Mg_2Si, white particles = Al–Cu–Fe).

nucleating below the surface and only emerging when already rather long.

The larger cracks detected in AA7449 were generally found to propagate along the grain boundaries of recrystallised grains (without much substructure) aligned along the transverse and longitudinal axes. Fig. 12(a) and (b) show two clear examples for samples aligned in the ST-L and ST-T orientation, respectively. These long cracks generally showed less segmentation and branching than cracks in AA7075. For example, the crack in Fig. 12(a) is a single, long crack along the full length. Furthermore, secondary cracks were only observed to occur along the interface of recrystallised grains, which in some cases were completely perpendicular to the crack plane (Fig. 12(a)). Additionally, the cracks deviate from the main crack propagation direction especially at the edges of recrystallised grains, also evident in Fig. 12(a). Similarly, many short cracks were found to nucleate at these recrystallised grain boundaries as shown in Fig. 12(c) and (d). It can therefore be concluded that the interface of recrystallised grains are more sensitive to HEAC.

From the etched crack sections in Fig. 12, different features were associated with crack arrest, including: grain boundary triple junctions, small particles and grain boundaries which were not perpendicular to the tensile axis (unfavourably oriented grain boundaries). For example, crack arrest at unfavourably oriented steep grain boundaries, resulting from the relatively equiaxed recrystallised grains, can be identified in Fig. 12(b),(c),(e); similar to the crack in Fig. 8 at location B. Small particles can also be seen to impede crack propagation in Fig. 12(b),(c),(e). This is in keeping with the fracture surface observations, where small constituent particles were uncracked and the opposite was true for coarse particles. In addition, cracks are also seen to stop at triple junctions in Fig. 12(b),(d), consistent with the EBSD map in Fig. 8.

4. Discussion

4.1. Surface blisters

Small black speckles (~ 2 µm diameter) appeared on the surface of both alloys after exposing the samples to the warm moist air. These are most likely blisters in the oxide film. This is based on observations made by Scamans et al. on AlZnMg alloys exposed to water vapour saturated air at 70°C [37]. They identified that the blisters formed because of the accumulation of hydrogen in the interface between the alumina layer and the matrix. Blistering has been found to occur preferentially at grain boundaries for AlZnMg alloys [37,38]. This is consistent with the fact that the propagating cracks surveyed in this investigation intersect many of the speckles. The process by which blisters produce locally reactive sites by damaging the passive layer may therefore be important in the HEAC process by increasing surface reaction rates and allowing the ingress of hydrogen. However, it must be checked whether this phenomenon occurs solely at high temperatures and hence if it is relevant at the operational temperatures of aircraft.

4.2. Crack morphology

The cracks of AA7075 were always perpendicular to the tensile axis

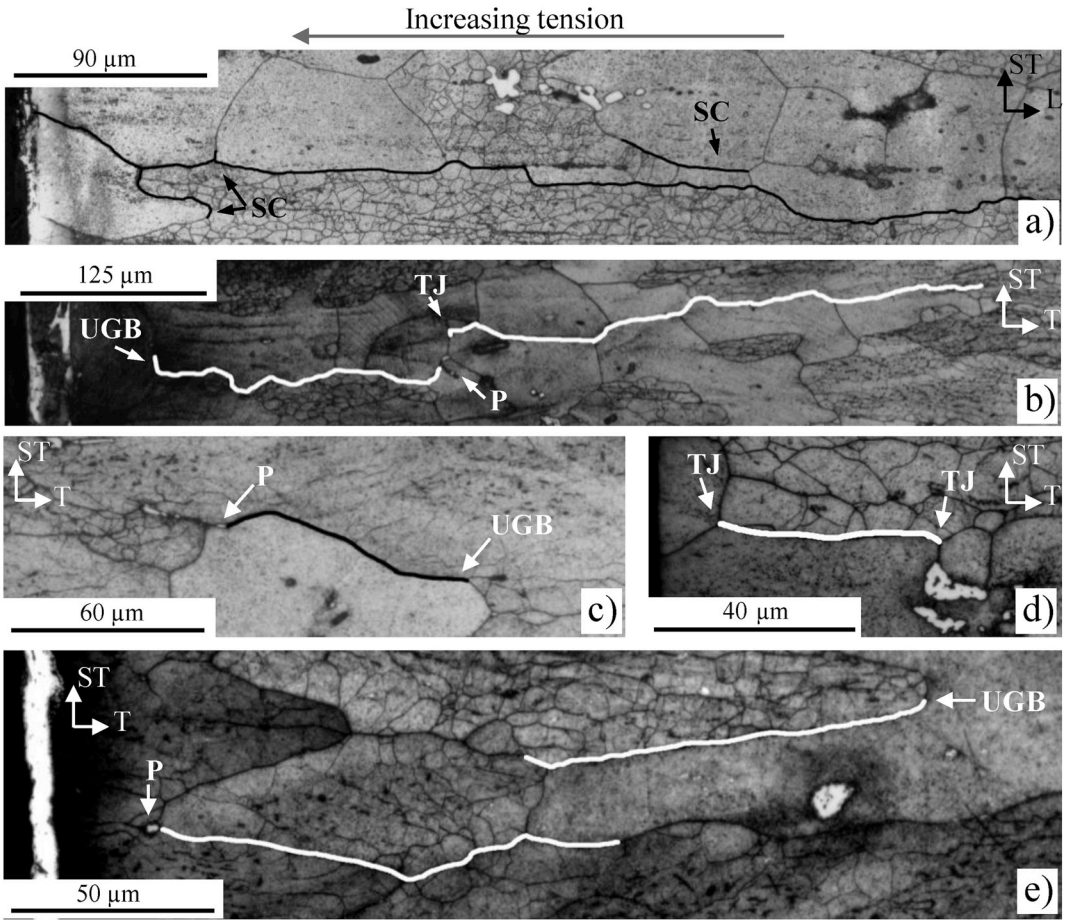

Fig. 12. Images showing the etched microstructure in sections of AA7449 samples containing cracks revealed by sequential polishing. The polishing was performed from the long edge of the samples (see region B in Fig. 3), such that the sample surface is to the left of each figure. Hence, the cracks are growing into the sample as they progress from left to right. The crack paths are outlined with solid lines. Labelled features: **SC** = secondary crack, **TJ** = triple junction, **P** = particle, **UGB** = unfavourably oriented grain boundary.

(Fig. 7), revealing the importance of a high resolved normal stress for cracking to proceed. Gruhl considered that the grain boundary can be treated as a 2D layer of low elastic modulus between grains of high elastic modulus, such that the transverse contraction is negligible [8]. Therefore, a correctly oriented grain boundary with a normal aligned with the tensile loading axis can result in a high hydrostatic stress, which is known to have a dominant role in HEAC [39]. This can be associated with a higher localised hydrogen content, which increases exponentially with hydrostatic stress due to lattice dilation [40]. Thus, HEAC cracks in 7xxx alloys are seen to preferentially form at grain boundaries perpendicular to the ST and tensile axes.

Cracks in AA7449 were found to have a much greater tortuosity, implying that growth could continue even when the resolved normal stress was relatively low. This shows that the grain boundaries in AA7449 are much more sensitive to HEAC. As a result, crack propagation in AA7449 was much faster than in AA7075 and cracks were less prone to crack arrest at microstructural features. The cracks surveyed in AA7449 at 300 MPa showed temporary crack arrest at triple junctions and unfavourably angled grain boundaries, but crack propagation resumed with extended exposure. In contrast, most cracks in AA7075 stopped growing altogether when they reached the end of a well-oriented boundary, particularly at stresses under 350 MPa. These observations can be correlated with the time to failure. At high stresses, AA7449 samples fractured very quickly as cracks could easily surpass barriers to growth. A second scenario is typical of AA7075 at high stress (>350 MPa) and AA7449 at 200–300 MPa. In this case there was a considerable delay in the appearance of macroscopic cracks. This can be associated to the halting of cracks at obstacles to growth, such as triple junctions, until the local resistance to crack growth has dropped sufficiently to allow progression. Finally, for samples at low stresses (<200 MPa for AA7449 and < 300 MPa for AA7075), macroscopic cracks were only observed after extended exposure times above 1600 h, as the nucleated cracks slowed down or stopped growing completely at even modest barriers to growth. Importantly, these samples still contain a significant number of short cracks, especially below the surface. Thus, the rate controlling step seems to be the growth of microstrucurally short cracks, and their transition to true long cracks, rather than their initial formation. As a consequence, the time to failure of both alloys change drastically from low to high stresses, as a high enough stress is essential to cause cracks to overcome barriers to growth and cause crack coalescence.

The ability of cracks in AA7449 to grow along boundaries not perpendicular to the loading axis also implies that cracks can grow to much larger sizes without segmenting. This can be contrasted with AA7075 where cracks were much more segmented. Burnett et al. investigated the segmented crack growth of a compact tension specimen of AA7032 exposed to an ambient environment using X-ray tomography [41]. They established that HEAC cracks in aluminium alloys are really colonies of coplanar cracks that are constantly branching and coalescing. As a result of ligaments from crack branching, the stress intensity at the crack tip is diminished, which significantly reduces the crack growth rate. The high susceptibility in AA7449 allows tortuous long cracks to grow with little branching. This in turn causes a reduction in crack segmentation, relative to AA7075, and preventing mutual crack

shielding. This further enhances crack growth rates in AA7449, or at least minimises opportunities for cracks to block each other's growth.

4.3. Microstructure

Different features were found to be responsible for crack arrest and initiation. Microcracks in AA7075 were mainly linked with coarse particles. It can be inferred that the coarse particles may have an important role in crack nucleation by providing stress concentration to nearby grain boundaries or influencing the surrounding microstructure. Bhuiyan et al. identified using X-ray tomography that crack initiation also occurred at cracked Al–Cu–Fe particles near the surface during monotonic tensile loading of AA7150 modified to contain high amounts of Zn and absorbed hydrogen [19]. The main features causing crack arrest were found to be small particles and triple junctions. As small particles did not fracture, they impeded crack growth. Some macroscopic cracks propagated through small particles through the decohesion of the particle-matrix interface. In the case of triple junctions, the cracks were seen to decelerate as they approached these features. After the cracks propagated through the triple junctions, crack growth resumed and accelerated as a larger portion of the grain boundary fractured. As a result, more elongated grains can be deduced to increase the sensitivity to HEAC. The ST-T samples were found to be generally more susceptible than ST-L samples. In the case of ST-T samples, the longitudinal axis is parallel to the maximum tension surface. For ST-L samples the longitudinal axis is perpendicular. Macroscopic surface cracks can grow faster than subsurface cracks as the fracture energy required is less. Therefore, since the grain boundary length in the crack propagation direction parallel to the surface is greater for ST-T samples, cracks encounter less triple junctions and crack growth is faster.

4.4. Subsurface cracking

Most of the cracks in AA7449 and AA7075 were seen to nucleate subsurface (at least 70% in a coupon of AA7075 and at least 78% in a coupon of AA7449). This has serious implications in the safety assessments of aircraft components, as most HEAC cracks are unlikely to be visible. Additionally, this reveals that HEAC cracks in moist air do not initiate from corrosion pits, as is understood for classical stress corrosion cracking [42]. Tsai and Chuang exposed statically loaded 2-pt. bend samples of AA7075 and AA7475 to an atmospheric environment (subjected to rain fall) [43]. It was identified that the initiation of cracks occurred via corrosion pits and crevices. Therefore, the crack initiation mechanism can differ depending on the aggressiveness and nature of the environment.

4.5. Sensitivity of AA7449

At first glance, AA7075 looks more liable to rapid crack growth than AA7449. The presence of broad flat grain boundaries (longer than 1 mm along the longitudinal direction) implies that the grain boundaries should have a higher resolved normal stress and that cracks can propagate longer distances without encountering barriers to growth [16]. On the contrary, AA7449 was established to be much more susceptible. Thus, it can be conjectured that the higher sensitivity of AA7449 cannot be attributed to the configuration of the microstructure, but rather a phenomenon at a smaller scale resulting from differences in the elemental composition of the alloys. Though understanding why grain boundaries in AA7449 are weaker is outside the scope of this paper, it must be noted that changes in the composition can cause differences in the size, composition and distribution of strengthening precipitates (matrix precipitates and grain boundary precipitates) and the precipitate free zone (PFZ). This in turn can have a drastic effect on hydrogen diffusion and the grain boundary electrochemistry [44,45]. As cracks were identified to nucleate mainly subsurface, it can be inferred that the grain boundary electrochemistry may not play a critical role during crack initiation. Additionally, the AA7449 was in an overaged condition (T7651), whereas the AA7075 was in a peak aged condition (T651). It is widely accepted that overaging in materials results in a higher resistance to HEAC [7]. This is because (a) coarser/incoherent precipitates with a high binding energy can result in irreversible hydrogen trapping which impede hydrogen diffusion [46] and (b) coarse particles are not easily sheared and can prevent coarse inhomogeneous slip that may facilitate hydrogen diffusion [24]. Thus, the greater susceptibility of AA7449 is unlikely to be caused by the internal hydrogen diffusion rates.

5. Conclusion

This study assessed the initiation and growth of microstructurally short cracks of AA7449 and AA7075 during static loading in moist air. The results found the following:

1. Modern alloys, like AA7449, are much more sensitive to HEAC than older alloys, like AA7075. This agrees with the recent bulletin of the European Aviation Safety Agency (EASA) [32].
2. A sample of AA7449 fractured in less than 704 h when loaded at 200 MPa (40% of yield) in 85% RH at 80°C. Fracture took only 24 h when the stress was closer to the yield point (>350 MPa). In contrast, AA7075 generally did not fracture after 1600 h even at 300 MPa and failure times were much greater even at stresses approaching yield.
3. Both alloys were found to produce large populations of microstructurally short cracks (<100 μm), associated with grain boundaries. Many more cracks were found below the surface, suggesting that surface examination may not be a safe method to evaluate propensity for cracking.
4. Failure was associated with a small number of extremely long cracks, that accelerated relative to the broader body of cracks, rather than by the gradual increase in length of the entire population.
5. The main distinction between AA7449 and AA7075 was the ability of cracks in the former to propagate in a much more tortuous manner and so propagate along unfavourably oriented boundaries or past triple points. Both were key arresting features for cracks in AA7075 and greatly reduced crack growth rates. As a result, cracks in AA7449 were less segmented and could grow faster, allowing a few cracks to quickly grow to several mm in length.

Data availability

The raw/processed data required to reproduce these findings cannot be shared at this time as the data also forms part of an ongoing study.

Declaration of competing interest

The authors declare that they have no known competing financial interests or personal relationships that could have appeared to influence the work reported in this paper.

Acknowledgement

I would like to acknowledge the Engineering and Physical Sciences Research Council (EPSRC) for providing funding in a Doctoral Training Partnership (DTP). This funding is provided for a PhD in the University of Bristol (UK). There is no available grant ID.

Appendix A. Supplementary data

Supplementary data to this article can be found online at https://doi.org/10.1016/j.msea.2019.138662.

References

[1] Y. Lee, R.P. Gangloff, Measurement and modeling of hydrogen environment–assisted cracking of ultra-high-strength steel, Metall. Mater. Trans. A 38 (2007) 2174–2190.
[2] B. Somerday, R. Gangloff, Effect of strength on environment-assisted cracking of ti–8v–6cr–4mo–4zr–3al in aqueous nacl: Part 1: Age hardening vs. work hardening, Mater. Sci. Eng. A 254 (1998) 166–178.
[3] H. Birnbaum, Mechanical properties of metal hydrides, J. Less Common Met. 104 (1984) 31–41.
[4] A.R. Troiano, The role of hydrogen and other interstitials in the mechanical behavior of metals, Metallography, Microstructure, and Analysis 5 (2016) 557–569.
[5] S. Lynch, Environmentally assisted cracking: overview of evidence for an adsorption-induced localised-slip process, Acta Metall. 36 (1988) 2639–2661.
[6] I.M. Robertson, P. Sofronis, A. Nagao, M. Martin, S. Wang, D. Gross, K. Nygren, Hydrogen embrittlement understood, Metall. Mater. Trans. A 46 (2015) 2323–2341.
[7] G.A. Young, J.R. Scully, The effects of test temperature, temper, and alloyed copper on the hydrogen-controlled crack growth rate of an al-zn-mg-(cu) alloy, Metall. Mater. Trans. A 33 (2002) 1167–1181.
[8] W. Gruhl, Stress corrosion cracking of high strength aluminium alloys, Zeitschrift fur Metalkunde 75 (1984) 819–826.
[9] N.H. Holroyd, G. Scamans, Crack propagation during sustained-load cracking of al-zn-mg-cu aluminum alloys exposed to moist air or distilled water, Metall. Mater. Trans. A 42 (2011) 3979–3998.
[10] S. Knight, K. Pohl, N. Holroyd, N. Birbilis, P. Rometsch, B. Muddle, R. Goswami, S. Lynch, Some effects of alloy composition on stress corrosion cracking in al–zn–mg–cu alloys, Corros. Sci. 98 (2015) 50–62.
[11] R.P. Wei, Fracture Mechanics: Integration of Mechanics, Materials Science and Chemistry, Cambridge University Press, 2010.
[12] H. Vogt, M. Speidel, Stress corrosion cracking of two aluminium alloys: a comparison between experimental observations and data based on modelling, Corros. Sci. 40 (1998) 251–270.
[13] S. Ciaraldi, J. Nelson, R. Yeske, E. Pugh, Hydrogen effects in metals, IM Bernstein and AW Thompson (1980) 437–447.
[14] N. Birbilis, R. Buchheit, Electrochemical characteristics of intermetallic phases in aluminum alloys an experimental survey and discussion, J. Electrochem. Soc. 152 (2005) B140–B151.
[15] M.O. Speidel, M.V. Hyatt, Stress-corrosion cracking of high-strength aluminum alloys, Advances in corrosion science and technology (1972) 115–335.
[16] M.O. Speidel, Stress corrosion cracking of aluminum alloys, Metall. Mater. Trans. A 6 (1975) 631–651.
[17] S. Knight, N. Birbilis, B. Muddle, A. Trueman, S. Lynch, Correlations between intergranular stress corrosion cracking, grain-boundary microchemistry, and grain-boundary electrochemistry for al–zn–mg–cu alloys, Corros. Sci. 52 (2010) 4073–4080.
[18] B. Sarkar, M. Marek, E. Starke, The effect of copper content and heat treatment on the stress corrosion characteristics of ai-6zn-2mg-x cu alloys, Metall. Mater. Trans. A 12 (1981) 1939–1943.
[19] M.S. Bhuiyan, Y. Tada, H. Toda, S. Hang, K. Uesugi, A. Takeuchi, N. Sakaguchi, Y. Watanabe, Influences of hydrogen on deformation and fracture behaviors of high zn 7xxx aluminum alloys, Int. J. Fract. 200 (2016) 13–29.
[20] M.A. Krishnan, V. Raja, Development of high strength aa 7010 aluminum alloy resistant to environmentally assisted cracking, Corros. Sci. 109 (2016) 94–100.
[21] W. Qi, R. Song, X. Qi, H. Li, Z. Wang, C. Wang, J. Jin, Hydrogen embrittlement susceptibility and hydrogen-induced additive stress of 7050 aluminum alloy under various aging states, J. Mater. Eng. Perform. 24 (2015) 3343–3355.
[22] Z. Chen, Y. Mo, Z. Nie, Effect of zn content on the microstructure and properties of super-high strength al-zn-mg-cu alloys, Metall. Mater. Trans. A 44 (2013) 3910–3920.
[23] B. Kannan, V. Raja, Hydrogen embrittlement susceptibility of over aged 7010 al-alloy, J. Mater. Sci. 41 (2006) 5495–5499.
[24] D. Nguyen, A. Thompson, I. Bernstein, Microstructural effects on hydrogen embrittlement in a high purity 7075 aluminum alloy, Acta Metall. 35 (1987) 2417–2425.
[25] L. Oger, M.C. Lafouresse, G. Odemer, L. Peguet, C. Blanc, Hydrogen diffusion and trapping in a low copper 7xxx aluminium alloy investigated by scanning kelvin probe force microscopy, Mater. Sci. Eng. A 706 (2017) 126–135.
[26] J.K. Park, A. Ardell, Effect of retrogression and reaging treatments on the microstructure of ai-7075-t651, Metall. Mater. Trans. A 15 (1984) 1531–1543.
[27] J. Burns, R. Bush, J. Ai, J. Jones, Y. Lee, R. Gangloff, Effect of water vapor pressure on fatigue crack growth in al–zn–cu–mg over wide-range stress intensity factor loading, Eng. Fract. Mech. 137 (2015) 34–55.
[28] M.V. Hyatt, Use of precracked specimens in stress corrosion testing of high strength aluminum alloys, Corrosion 26 (1970) 487–503.
[29] K. Ural, A study of optimization of heat-treatment conditions in retrogressions and reageing treatment of 7075-t6 aluminium alloy, J. Mater. Sci. Lett. 13 (1994) 383–385.
[30] S. Sakai, N. Nakajima, M. Kamaya, A study of evaluation method for life time of alloy 600 on primary water stress corrosion cracking, Corrosion 2001 (2001).
[31] T. Dursun, C. Soutis, Recent developments in advanced aircraft aluminium alloys, Mater. Des. 56 (2014) 862–871.
[32] EASA, Environmentally assisted cracking in certain aluminium alloys, European Aviation Safety Agency, Safety Information Bulletin 2018–04R1 (2018). https://ad.easa.europa.eu/ad/2018-04R1.
[33] A. International, Standard practice for preparation and use of bent-beam stress-corrosion test specimens, Corrosion of Metals; Wear and Erosion 03 (2016) G39–G99.
[34] J. Robson, P. Prangnell, Modelling al3zr dispersoid precipitation in multicomponent aluminium alloys, Mater. Sci. Eng. A 352 (2003) 240–250.
[35] H. Fang, H. Chao, K. Chen, Effect of zr, er and cr additions on microstructures and properties of al–zn–mg–cu alloys, Mater. Sci. Eng. A 610 (2014) 10–16.
[36] Y. Zhang, C. Bettles, P.A. Rometsch, Effect of recrystallisation on al 3 zr dispersoid behaviour in thick plates of aluminium alloy aa7150, J. Mater. Sci. 49 (2014) 1709–1715.
[37] G. Scamans, A. Rehal, Electron metallography of the aluminium-water vapour reaction and its relevance to stress-corrosion susceptibility, J. Mater. Sci. 14 (1979) 2459–2470.
[38] L. Christodolou, H. Flower, In-situ h.v.e.m. observations of hydrogen embrittlement, Hydrogen Effects in Metals (1980) 493–501.
[39] R. Gangloff, Hydrogen-assisted Cracking. Comprehensive Structural Integrity, vol. 6, Elsevier, Oxford, 2003. Environmentally-Assisted Fracture.
[40] E. Martínez-Pañeda, C.F. Niordson, R.P. Gangloff, Strain gradient plasticity-based modeling of hydrogen environment assisted cracking, Acta Mater. 117 (2016) 321–332.
[41] T.L. Burnett, N.H. Holroyd, G.M. Scamans, X. Zhou, G.E. Thompson, P.J. Withers, The role of crack branching in stress corrosion cracking of aluminium alloys, Corros. Rev. 33 (2015) 443–454.
[42] H. Hänninen, Stress Corrosion Cracking. Comprehensive Structural Integrity, vol. 6, Elsevier, Oxford, 2003. Environmentally-Assisted Fracture.
[43] T. Tsai, T. Chuang, Atmospheric stress corrosion cracking of a superplastic 7475 aluminum alloy, Metall. Mater. Trans. A 27 (1996) 2617–2627.
[44] R. Goswami, S. Lynch, N.H. Holroyd, S.P. Knight, R.L. Holtz, Evolution of grain boundary precipitates in al 7075 upon aging and correlation with stress corrosion cracking behavior, Metall. Mater. Trans. A 44 (2013) 1268–1278.
[45] N. Birbilis, M. Cavanaugh, R. Buchheit, Electrochemical behavior and localized corrosion associated with al 7 cu 2 fe particles in aluminum alloy 7075-t651, Corros. Sci. 48 (2006) 4202–4215.
[46] M.S. Bhuiyan, H. Toda, Z. Peng, S. Hang, K. Horikawa, K. Uesugi, A. Takeuchi, N. Sakaguchi, Y. Watanabe, Combined microtomography, thermal desorption spectroscopy, x-ray diffraction study of hydrogen trapping behavior in 7xxx aluminum alloys, Mater. Sci. Eng. A 655 (2016) 221–228.